# OBSERVATIONS AND MODELING OF THE INNER DISK REGION OF T TAURI STARS

R. L. AKESON,[1] C. H. WALKER,[2] K. WOOD,[2] J. A. EISNER,[3] E. SCIRE,[4] B. PENPRASE,[4]
D. R. CIARDI,[1] G. T. VAN BELLE,[1] B. WHITNEY,[5] AND J. E. BJORKMAN[6]

## ABSTRACT

We present observations of four T Tauri stars using long baseline infrared interferometry from the Palomar Testbed Interferometer. The target sources, T Tau N, SU Aur, RY Tau, and DR Tau, are all known to be surrounded by dusty circumstellar disks. The observations directly trace the inner regions ($<1$ AU) of the disk and can be used to constrain the physical properties of this material. For three of the sources observed, the infrared emission is clearly resolved. We first use geometric models to characterize the emission region size, which ranges from 0.04 to 0.3 AU in radius. We then use Monte Carlo radiation transfer models of accretion disks to jointly model the spectral energy distribution and the interferometric observations with disk models including accretion and scattering. With these models, we are able to reproduce the data set with extended emission arising from structures larger than 10 mas contributing less than 6% of the $K$-band emission, consistent with little or no envelope remaining for these class II sources [$d \log (\lambda F_\lambda)/d \log \lambda \approx -2-0$ in the infrared]. The radiation transfer models have inner radii for the dust similar to the geometric models; however, for RY Tau, emission from gas within the inner dust radius contributes significantly to the model flux and visibility at infrared wavelengths. The main conclusion of our modeling is that emission from inner gas disks (between the magnetic truncation radius and the dust destruction radius) can be a significant component in the inner disk flux for sources with large inner dust radii.

*Subject headings:* circumstellar matter — infrared: stars — planetary systems: protoplanetary disks — techniques: high angular resolution

*Online material:* color figures

## 1. INTRODUCTION

In the canonical model, T Tauri systems comprise the central star, a rotating disk of gas and dust, a jet or outflow, and possibly a residual circumstellar envelope (see, e.g., Bertout 1989). In many cases, the central star is still accreting material, and this process, as well as the mechanisms driving the outflow, are dependent on and influence the properties of the inner disk ($<1$ AU). Several groups (e.g., Koenigl 1991; Shu et al. 1994) have proposed models in which the stellar magnetic field truncates the disk at a few stellar radii. Matter from the disk flows along the field lines and onto the star, producing hot spots or rings that can explain observed ultraviolet photometric variability (Kenyon et al. 1994; Wood et al. 1996; Gomez de Castro & Franqueira 1997).

In the last several years, the technique of long baseline infrared interferometry has been applied to the study of circumstellar material around young stellar objects. These observations are sensitive to hot material near the star itself. Given the milliarcsecond resolution capability of the current generation of interferometers, these observations can, in many cases, spatially resolve the emission from the hot (a few thousand Kelvin) ma-

terial and are well suited for observations of the inner regions of young stellar objects. The first young stellar object to be observed using this technique was FU Ori (Malbet et al. 1998), followed by Herbig Ae/Be stars (Millan-Gabet et al. 1999, 2001) and T Tauri stars (Akeson et al. 2000, hereafter Paper 1). The FU Ori results were consistent with accretion disk models, while both the T Tauri and Herbig star results found characteristic sizes larger than expected from geometrically flat accretion disk models. More recent observations of Herbig objects (Eisner et al. 2004) have found earlier spectral type objects that are consistent with accretion disk predictions.

Measurements of the spectral energy distribution (SED) at optical through radio wavelengths probe a range of processes in young stellar objects, including the stellar photosphere, accretion onto the star or disk, emission from gas and dust in the disk, and emission from the outflow. In many sources, continuum emission from circumstellar or accreting material adds to the stellar spectrum, decreasing the stellar spectral features in an effect called veiling. For T Tauri stars, the veiling in the infrared can be very high, indicating substantial excess emission (see, e.g., Folha & Emerson 1999).

In Paper 1 we presented observations showing that the infrared emission from the T Tauri stars T Tau N and SU Aur is resolved. The visibilities from T Tauri stars can be difficult to model, given the substantial stellar component, infrared variability, and possible presence of a significant extended component. In this paper, we present further interferometric observations of the T Tauri stars T Tau N, SU Aur, DR Tau, and RY Tau using the Palomar Testbed Interferometer (PTI) and infrared photometry from the Pomona College 1 m telescope. In § 4, we present geometric models to constrain the emission size and orientation. In § 5, we present detailed source models that include the scattered light and reprocessing of starlight and dissipation of viscous

[1] Michelson Science Center, California Institute of Technology, MS 100-22, Pasadena, CA 91125.
[2] School of Physics and Astronomy, University of St Andrews, North Haugh, St Andrews, KY16 9AD, UK.
[3] Department of Astronomy, California Institute of Technology, MS 105-24, Pasadena, CA 91125.
[4] Department of Physics and Astronomy, Pomona College, Claremont, CA 91711.
[5] Space Science Institute, 3100 Marine Street, Suite A353, Boulder, CO 80303.
[6] Ritter Observatory, Department of Physics and Astronomy, University of Toledo, Toledo, OH 43606.

## TABLE 1
### Stellar Parameters for the Observed Sources

| Source | Spectral Type | $L_*$ ($L_\odot$) | $R_*$ ($R_\odot$) | Reference |
|---|---|---|---|---|
| T Tau N..... | K0 | 7.3 | 2.8 | White & Ghez (2001) |
| SU Aur...... | G2 | 12.9 | 3.5 | Muzerolle et al. (2003) |
| DR Tau...... | K7 | 0.87 | 1.9 | Muzerolle et al. (2003) |
| RY Tau...... | K1 | 12.8 | 3.6 | Muzerolle et al. (2003) |

## TABLE 3
### Calibrators for T Tau Sources from PTI

| Calibrator | Diameter Estimate (mas) | Sources |
|---|---|---|
| HD 28024 .... | 0.68 | T Tau N, SU Aur, DR Tau, RY Tau |
| HD 30111..... | 0.60 | T Tau N, SU Aur |
| HD 30122 .... | 0.11 | T Tau N, SU Aur |
| HD 28677 .... | 0.34 | DR Tau, RY Tau |
| HD 26737 .... | 0.24 | DR Tau, RY Tau |

accretion energy in the disk to fit both the SED and the infrared visibilities.

## 2. SOURCES

All four sources are located in the Taurus-Auriga molecular cloud (distance ∼140 pc) and are well-studied T Tauri objects. Source spectral types and stellar properties given in Table 1 are taken from recent references using infrared spectroscopy. Given the sensitivity restrictions of PTI, we have chosen sources that are among the most infrared luminous T Tauri objects. As the PTI acquisition system works in the optical, there is a selection effect against highly inclined, optically obscured sources.

All four systems have significant emission in excess of the stellar photosphere from near infrared through millimeter wavelengths, and all are believed to have circumstellar disks. The T Tau system comprises the optically visible star T Tau N and its infrared companion T Tau S, which is itself a binary (Koresko 2000). The PTI observations are of T Tau N, the component that dominates the millimeter emission (Akeson et al. 1998). SU Aur has an SED similar to that of T Tau N, although Herbig & Bell (1988) classified SU Aur separately from other T Tauri stars because of its high luminosity and broad absorption lines. RY Tau is associated with a reflection nebulosity (Nakajima & Golimowski 1995) and has millimeter-wave molecular line emission consistent with a Keplerian disk (Koerner & Sargent 1995). DR Tau is one of the most heavily veiled T Tauri stars and is highly variable in the optical (Gullbring et al. 2000) and near-infrared (Kenyon et al. 1994).

## 3. OBSERVATIONS

### 3.1. *Infrared Interferometry*

Infrared interferometry data were taken at the Palomar Testbed Interferometer (PTI), which is described in detail by Colavita et al. (1999). PTI is a long-baseline, direct-detection interferometer that uses active fringe tracking in the infrared. Data presented here were obtained in the $K$ band (2.2 $\mu$m) in all three PTI baselines: NS (110 m), NW (85 m), and SW (85 m). In our analysis below, we also use the SU Aur observations described in Akeson et al. (2002) and Paper 1. A summary of the

new observations is given in Table 2. These data were acquired over a period from 2001 September 24 to 2003 October 16. The data in the NS and NW baselines were taken with a 20 ms fringe integration time, while the SW data were taken with a 50 ms time, providing better S/N for these data.

The data were calibrated using the standard PTI method (Boden et al. 1998). Briefly, a synthetic wide-band channel is formed from five spectrometer channels ($\lambda = 2.0–2.4$). The system visibility, the response of the interferometer to an unresolved object, is measured using calibrator stars. The calibrator star sizes were estimated using a blackbody fit to photometric data from the literature and were checked to be internally consistent. Calibrators were chosen for their proximity to the source and for small angular size, minimizing systematic errors in deriving the system visibility. All calibrators used here have angular diameters <0.7 mas and were assigned uncertainties of 0.1 mas (Table 3). The calibrated data are presented in normalized squared visibility ($V^2 = 1$ for an unresolved source), which we refer to as visibility in this paper. The calibrated visibility uncertainties are a combination of the calibrator size uncertainty and the internal scatter in the data. As DR Tau is near the tracking limit for PTI, the wide-band data are used rather than the synthetic wide-band (spectral channel) data. The main difference between these two channels is that the spectral channels are spatially filtered, and the wide-band channel is not. The accuracy of the wide-band data was confirmed by comparing the wide-band and synthetic wide-band data for other sources observed on the same night as DR Tau.

The calibrated data were edited to remove integrations with very high jitter (a measure of the phase noise) and integrations for which the estimates of the system visibility from separate calibrator observations disagreed by more than 3 $\sigma$. In general, the points eliminated were from entire nights with marginal weather or integrations taken at large hour angles. No more than 10% of the data for any given source was removed, except for DR Tau on the NS baseline, and inclusion of these data points would not substantially change the results given below.

The calibrated and edited data are shown in Figure 1 for each source as a function of projected baseline length and position

## TABLE 2
### New Observations of T Tau Sources from PTI

| Source | NS | | NW | | SW | |
|---|---|---|---|---|---|---|
| | Nights | Integrations | Nights | Integrations | Nights | Integrations |
| T Tau N......... | . . . | . . . | . . . | . . . | 1 | 6 |
| SU Aur........... | . . . | . . . | . . . | . . . | 1 | 6 |
| DR Tau........... | 3 | 5 | 1 | 3 | 1 | 4 |
| RY Tau........... | 4 | 27 | 3 | 14 | 2 | 8 |

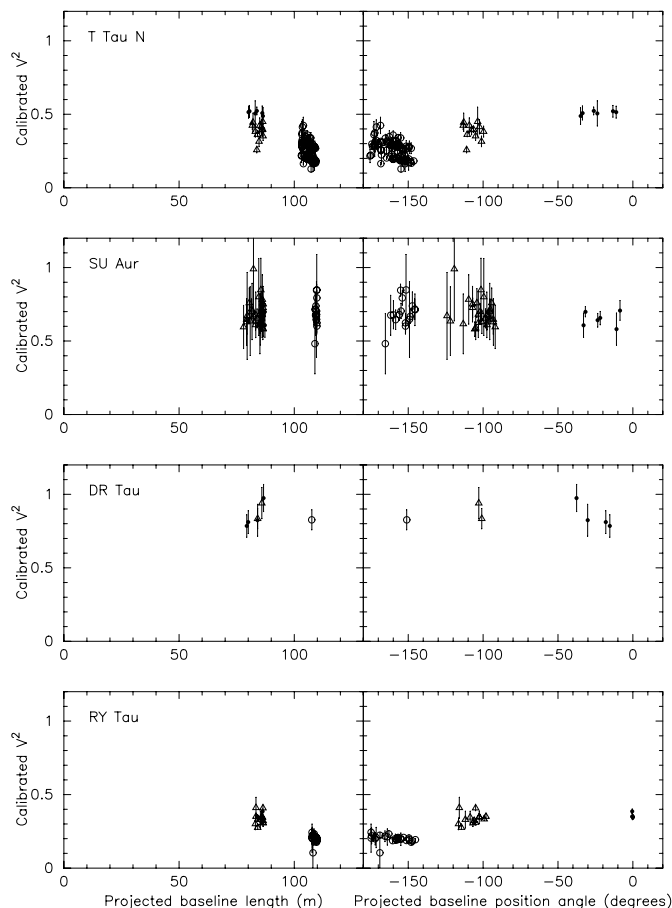Note.—Each integration represents 125 s of fringe data.

Fig. 1.—Calibrated PTI visibilities for each of the four sources by baseline: NS (*open circles*), NW (*open triangles*), and SW (*filled circles*). For T Tau N and SU Aur, the data from Akeson et al. (2002) are also plotted. [*See the electronic edition of the Journal for a color version of this figure.*]

angle. Three of the four sources, T Tau N, SU Aur, and RY Tau, are clearly resolved. The new observations of T Tau N are consistent with the results of Akeson et al. (2002). We have not calculated models for T Tau N here; scattered light models of T Tau N that reproduce the observed asymmetry (Stapelfeldt et al. 1998) are detailed in Wood et al. (2001).

### 3.2. *Infrared Photometry*

A sample of young stellar objects, including DR Tau, SU Aur, and RY Tau and a sequence of photometric standard stars taken from Landolt (1992), were observed over seven nights from 2003 December to 2004 March (December 16, January 10, 13, 15, 22, and 23, and March 9) using the Pomona College 1 m telescope with the Claremont-Riverside Infrared Camera (CLIRCAM) in the $J$ and $K$ bands. For each object, a series of at least five dithered exposures was used to create individual sky images for each field. The sky background and instrumental noise were subtracted from all the images, and repeat exposures were median combined after shifting to a common astrometric reference frame to remove a majority of the background noise. Instrumental magnitudes were converted to standard $J$ and $K$ magnitudes using a combination of the published magnitudes and the $J$ and $K$ magnitudes from bright Two Micron All Sky Survey (2MASS) stars in the image frames. The magnitudes given in Table 4 are the average magnitudes over all six nights using the average calibration zero points from the complete sample of photometric standards and 2MASS stars. The three sources observed showed no statistically significant variability over the nights observed and were constant in magnitude within the photometric error of 0.15 mag in $J$ and 0.15 mag in $K$. For comparison, the 2MASS $J$ and $K$ magnitudes and observation date are also given. Together, the Pomona and 2MASS data bracket the PTI observations. At the $K$ band, only RY Tau shows a significant difference between the 2MASS measurement and our more recent observations; however, past observations of these sources have shown infrared variability (particularly DR Tau; Kenyon et al. 1994). Additional information on the infrared observations from Table 4 will be presented in B. Penprase et al. (2005, in preparation).

### 4. GEOMETRIC MODELS

In this section, we discuss geometric models for SU Aur, RY Tau, and DR Tau. As PTI is a direct-detection interferometer, any emission within the $1''$ Gaussian (FWHM) field of view (FOV) will contribute to the measured visibility. As discussed in Akeson et al. (2002), there are many scenarios that could produce a visibility of less than 1. These include additional point sources within the field of view, a resolved source of emission, or extended (overresolved) emission, which would contribute incoherently. Any possible incoherent contribution (in this case, any emission on scales greater than 10 mas and within the $1''$ FOV) is hard to assess for our sources, given that many observations of envelopes or reflection nebulae do not include the central arcsecond because of contamination from the star itself. None of these three sources has a known companion within $1''$. DR Tau was included in lunar occultation observations of Simon et al. (1999), and no detection was reported with a point source–limiting magnitude of $\Delta K = 2.5$. Models including scattered light contributions are presented in § 5, and extended components are discussed in § 5.3.

TABLE 4
RESULTS OF INFRARED PHOTOMETRY OBSERVATIONS

| Source | No. of Nights | Magnitude | rms | 2MASS Magnitude | 2MASS rms | 2MASS Date |
|---|---|---|---|---|---|---|
| | | | *J* Band | | | |
| SU Aur................ | 6 | 7.24 | 0.143 | 7.20 | 0.020 | 1998 Jan 30 |
| DR Tau................ | 6 | 8.75 | 0.195 | 8.84 | 0.024 | 1997 Oct 10 |
| RY Tau................ | 5 | 7.52 | 0.226 | 7.15 | 0.019 | 1997 Oct 29 |
| | | | *K* Band | | | |
| SU Aur................ | 6 | 6.17 | 0.114 | 5.99 | 0.022 | 1998 Jan 30 |
| DR Tau................ | 6 | 6.87 | 0.183 | 6.87 | 0.017 | 1997 Oct 10 |
| RY Tau................ | 6 | 5.76 | 0.168 | 5.39 | 0.022 | 1997 Oct 29 |

For the model fitting in this section, we adopt a configuration of an unresolved point source (these stars have diameters ≤0.1 mas and therefore a $V^2 > 0.99$ at PTI) and a resolved component. We take the contribution of the stellar component from measurements of the infrared veiling. For SU Aur and DR Tau, we use the $K$-band veiling measurements of Muzerolle et al. (2003). For RY Tau, the Muzerolle et al. (2003) value of $r_K = 0.8 \pm 0.3$ (where $r_K = F_{excess}/F_{star}$) is much less than the lower limit of $r_K > 2.5$ from Folha & Emerson (1999). For our adopted model (point source plus resolved component), the PTI data and a value of $r_K = 0.8$ are incompatible (i.e., the point source contribution cannot be that large and still produce the PTI measurement), and we therefore use $r_K = 2.5 \pm 1$ for RY Tau in the geometric fits.

Simple geometric models of the emission are used to characterize the source size and inclination. The two models presented here use a uniform disk and a thin ring to represent the emission profile. For the uniform disk, only the measured visibility was used to determine the disk radius. For the ring model, visibilities were calculated for a range of inner diameters and compared to the observed visibilities. For each ring diameter considered, the width was determined by matching the excess flux, derived using the measured $K$-band veiling, with a blackbody emission source at a temperature of 1600 K, the assumed dust destruction temperature (Duschl et al. 1996). In these models, the dust destruction temperature controls the width of the ring but affects the fit radius only through the shape of the model visibility curve. For example, changing the blackbody temperature of the ring from 1200 to 2000 K would change the fit radius for RY Tau by 30%. Both face-on and inclined geometries were fit to the data (Table 5). The uncertainties in the model fits due to the uncertainty in the stellar contribution are also given.

The ring model fits are graphically shown in Figure 2. In this sky-plane representation, the radial coordinate for each data point is the inner ring size corresponding to the measured visibility and accounting for the stellar component listed in Table 5. The error bars include the errors on the data points but not the uncertainty in the stellar contribution. The polar coordinate is determined by the projected baseline position angle. In this way, the constraint provided by the data on both the size and the inclination are visible. The best-fit face-on and inclined ring models are also plotted.

### 4.1. Discussion

Using the simple geometric models, we find source sizes ranging from 0.04 to 0.3 AU in radius. As discussed in Paper 1 and by Millan-Gabet et al. (2001), the measured sizes for T Tauri stars and Herbig Ae stars were larger than expected from simple disk models. An explanation for this discrepancy in Herbig stars was proposed independently by two groups based on SED modeling (Natta et al. 2001) and aperture-masking observations (Tuthill et al. 2001). In these models, the inner edge of the dust disk is located at the radius where the dust reaches the sublimation temperature ($R_{dust}$). This configuration produces a vertically extended inner wall, reproducing both the SED and the interferometry observations for the Herbig sources. Dullemond et al. (2001) also applied this model to T Tauri stars. Further work by Muzerolle et al. (2003) extended the model to include the accretion luminosity as well as the stellar luminosity in determining the dust destruction radius for several T Tauri stars, including the three shown in Figure 2. In all these models, optically thin gas may be present within $R_{dust}$ (we discuss this point further in § 5.4).

We chose a ring distribution as a simple representation of a model in which the infrared emission arises from the inner wall

TABLE 5
Results from Geometric Model Fits

| Parameter | SU Aur | DR Tau | RY Tau |
|---|---|---|---|
| $f_{excess}$ [a] ............................ | $0.44 \pm 0.09$ | $0.8 \pm 0.3$ | $0.71 \pm 0.11$ |
| $K_m$ (2MASS) .................. | 5.99 | 6.87 | 5.40 |
| Face-on Models | | | |
| Uniform disk: | | | |
| Radius (AU) .............. | $0.20 \pm 0.028$ | $0.10 \pm 0.029$ | $0.29 \pm 0.036$ |
| $\sigma_v$ (AU) [b] .................... | 0.042 | 0.004 | 0.080 |
| $\chi^2$/dof ........................ | 2.5 | 0.85 | 2.9 |
| Ring: | | | |
| Inner radius (AU) ...... | $0.13 \pm 0.021$ | $0.057 \pm 0.027$ | $0.17 \pm 0.01$ |
| Width (AU) ............... | 0.050 | 0.028 | 0.035 |
| $\sigma_v$ (AU) [b] .................... | 0.036 | 0.010 | 0.059 |
| $\chi^2$/dof ........................ | 2.5 | 0.85 | 4.6 |
| Inclined Models | | | |
| Uniform disk: | | | |
| Radius (AU) .............. | $0.27 \pm 0.037$ | $0.11 \pm 0.03$ | $0.30 \pm 0.008$ |
| PA (deg) ..................... | $112 \pm 24$ | $160 \pm 55$ | $98 \pm 40$ |
| Inclination (deg) ......... | $51 \pm 11$ | $40 \pm 30$ | $19 \pm 6$ |
| $\chi^2$/dof ........................ | 0.9 | 0.77 | 2.3 |
| Ring: | | | |
| Inner radius (AU) ...... | $0.18 \pm 0.025$ | $0.070 \pm 0.026$ | $0.19 \pm 0.01$ |
| Width (AU) ............... | 0.008 | 0.019 | 0.029 |
| PA (deg) ..................... | $114 \pm 23$ | $160 \pm 55$ | $110 \pm 22$ |
| Inclination (deg) ......... | $52 \pm 10$ | $40 \pm 30$ | $25 \pm 3$ |
| $\chi^2$/dof ........................ | 0.9 | 0.78 | 3.0 |

[a] $f_{excess} = F_{excess}/F_{total}$, where $F_{total} = F_{star} + F_{excess}$.
[b] The systematic error, $\sigma_v$, is from the uncertainty in the stellar contribution.

of the dust disk. The values for $R_{dust}$ predicted by Muzerolle et al. (2003) are larger than our fit ring radii by roughly a factor of 2. We note that the presence of extended emission, which was not included in our model, would decrease the fit radius and therefore increase this discrepancy. The fit ring radii for SU Aur and RY Tau correspond to $10R_*$ and $11R_*$, much larger than the expected magnetic truncation radius ($3R_*$–$5R_*$; Shu et al. 1994). In § 5 we show that emission from gas between the magnetic truncation radius and $R_{dust}$ can reconcile accretion disk models with our observations.

The position angle coverage of the PTI data allows us to constrain the inclination of infrared emission. The $\chi^2$/dof improves substantially for SU Aur and RY Tau for the inclined models as compared to the face-on models, but the DR Tau data do not provide a good constraint on the inclination, given the large error bars, and because the source is at best marginally resolved. For RY Tau, our inclination angle of $19°$–$25°$ agrees with that derived by Koerner & Sargent (1995) from resolved millimeter emission ($25°$). However, the position angle (PA) is not well constrained by our data ($98° \pm 40°$ for the uniform disk and $110° \pm 22°$ for the ring) and does not agree with the PA of the millimeter emission ($48° \pm 5°$, Koerner & Sargent 1995; $27° \pm 7°$, Kitamura et al. 2002) and is not orthogonal to the jet PA of $110°$ from K. Stapelfeldt et al. (2005, in preparation). Our inclination angle of $52° \pm 10°$ agrees with the $60°$ estimate of Unruh et al. (2004) based on the photometric period and line widths. Muzerolle et al. (2003) find high ($86°$) inclination values for both RY Tau and SU Aur, which are not supported by the PTI data, particularly for RY Tau, and are also inconsistent with the low visible extinctions ($A_v = 2.1$ and $0.9$, respectively). At such high viewing angles, the star would be occulted
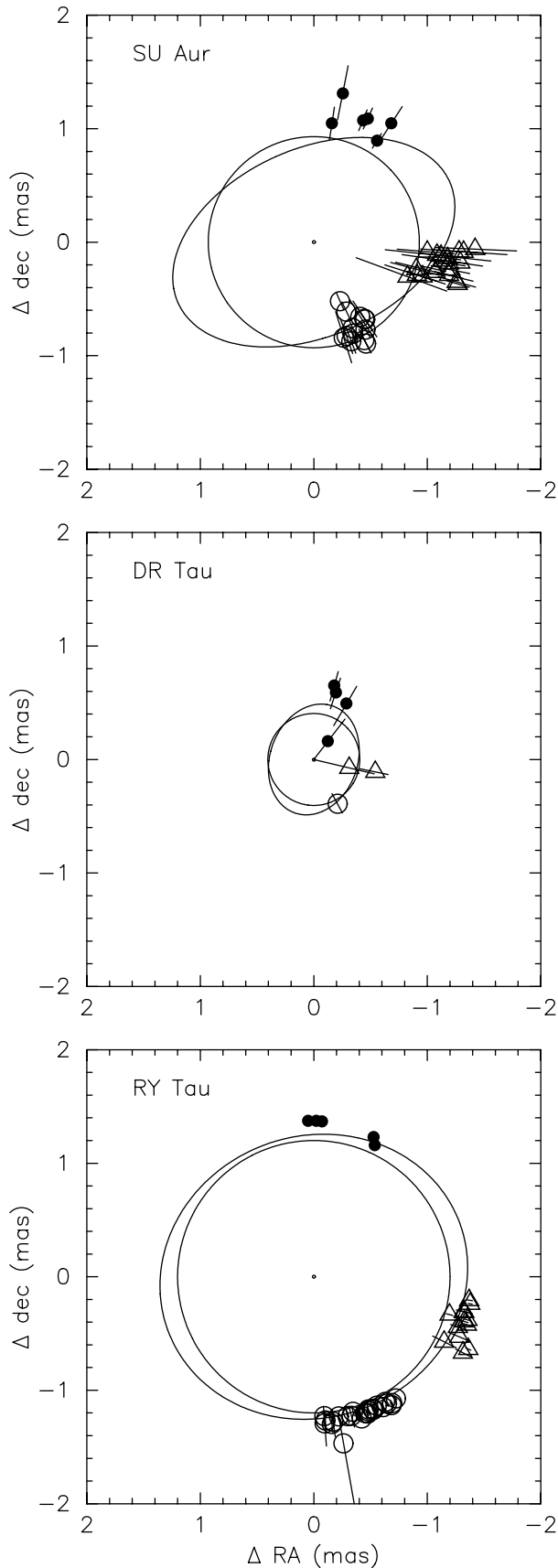
FIG. 2.—Data and uniform disk fits for the best-fit face-on and inclined models. An unresolved stellar component is included, as described in § 4. Separate symbols are used for each baseline: NS (*open circles*), NW (*open triangles*), and SW (*filled circles*). [*See the electronic edition of the Journal for a color version of this figure.*]

by the flared circumstellar disk. If there is a large incoherent component for any of the sources, then our simple geometric fits will underestimate the inclination angle, as an incoherent contribution is independent of baseline. However, in our detailed models (§ 5) for these three objects, the extended light contribution is less than 10%, which is insufficient to change the measured RY Tau inclination by 60°.

## 5. DETAILED RADIATION TRANSFER MODELS

One of the major uncertainties in the simple fits presented above is the assumption of no extended emission within the 1″ PTI FOV. To address this issue directly, we have calculated radiative transfer models for SU Aur, DR Tau, and RY Tau. The input properties are given in Table 1, and the goal is to match the PTI data and the SED.

### 5.1. *Monte Carlo Radiation Transfer Code*

We use the Monte Carlo radiative equilibrium technique of Bjorkman & Wood (2001), updated by C. Walker et al. (2005, in preparation), to self-consistently model each of our target sources. This code iteratively solves for the disk density structure, assuming the dust and gas are well mixed with a standard gas to dust ratio of 100 : 1 and the system is in vertical hydrostatic equilibrium. In addition to stellar irradiation, the code includes accretion and shock/boundary layer luminosity calculations according to Calvet & Gullbring (1998). Multiple scattering is treated alongside the heating and reprocessing of photons in the disk. Output data can be used to produce synthetic SEDs and multiwavelength images for any viewing angle of the disk system. For a more detailed description of the code and its updates, see Wood et al. (2002a, 2002b), Whitney et al. (2003a), 2003b), C. Walker et al. (2005, in preparation), and references therein.

The code computes the flared density structure of a steady accretion disk extending from the inner dust destruction radius to a specified outer radius (Fig. 3). The Monte Carlo technique naturally accounts for radiation transfer effects and the heating and hydrostatic structure of the inner wall of the dust disk. The vertical height of the inner wall of dust is not preset but rather calculated as part of the modeling process. For these models, the scale height of the density distribution is $0.3R_*$–$0.7R_*$ at the inner edge. The position of the inner dust disk edge, $R_{dust}$, is determined from the destruction temperature of silicates, taken to be 1600 K (Duschl et al. 1996). Within the disk, we adopt the dust-size distribution used for the modeling of HH 30 IRS and GM Aur (Wood et al. 2002a; Schneider et al. 2003; Rice et al. 2003). With a distribution of grain sizes or compositions, the dust destruction may take place over a range of radii, but this is beyond the scope of our work. Monnier & Millan-Gabet (2002) discuss the constraints on the dust properties from infrared interferometry observations.

In order to match the new PTI observations, for some sources $R_{dust}$ was large enough (>0.2 AU) that continuum emission from gas within $R_{dust}$ becomes significant. The structure and temperature of the gas disk is not computed self-consistently in our models. Instead, accretion luminosity is emitted following the temperature structure of an optically thick accretion disk (e.g., Lynden-Bell & Pringle 1974; Pringle 1981),

$$T_{gas}(R) = \left(\frac{3GM_*\dot{M}}{8\pi\sigma R^3}\right)\left[\left(1 - \sqrt{R_*/R}\right)^{1/2}\right]^{1/4}, \quad (1)$$

where $R$ is the radial distance in the midplane. The gas disk is assumed to be infinitely thin, so after being emitted, the
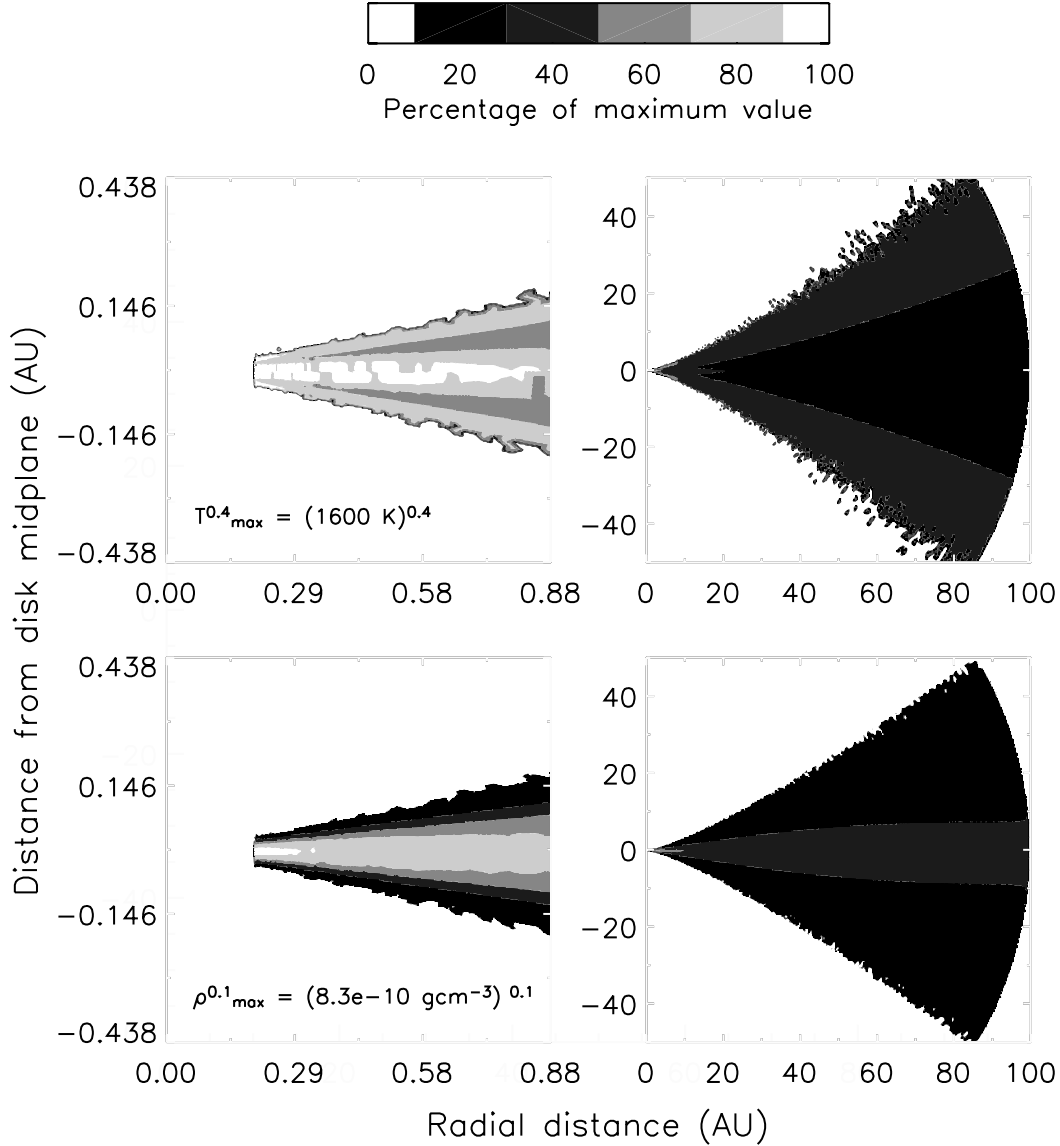
Fig. 3.—Temperature and density distributions for an example disk model. The top images are temperature scaled to the 0.5 power, and the bottom ones are density scaled to the 0.1 power. Note that the geometrically thin gas is not shown.

"accretion photons" do not encounter any opacity in the gas but may be scattered and absorbed and produce heating in the dust disk. Clearly, this is a simplification for the gas emission but is sufficient for our models. The assumed geometry of the gas disk is supported by recent modeling by Muzerolle et al. (2004) of Herbig Ae/Be sources in which the gas disk is geometrically thin, allowing direct radiation of the inner dust disk. Future work will investigate the effects of possible shielding of the dust disk by a flared, and possibly optically thick, inner gas disk.

The gas disk extends down to the magnetic truncation radius ($R_{gas}$), at which point material is thought to be channeled along magnetic field lines onto the star at a high-latitude shock zone (e.g., D'Alessio 2004; Kenyon et al. 1994). We assume that the gas disk is truncated at a magnetospheric radius dependent on the stellar radius, mass, accretion rate, and surface magnetic field (Ghosh & Lamb 1979). For DR Tau and RY Tau, we assume kilogauss magnetic fields and truncate the gas disk at $5R_*$. For SU Aur, thought to be more weakly magnetic and with inconclusive evidence for hot spots (Unruh et al. 2004), we use $2R_*$ for

$R_{gas}$. We assume that photons emitted from the shock/boundary layers have a spectrum of an 8000 K Planck function (Calvet & Gullbring 1998) and are emitted along with stellar photons, as in Muzerolle et al. (2003).

For each model, the stellar luminosity has been fixed, as detailed in Table 1, and for input stellar spectra we use the appropriate Kurucz (1994) model atmosphere. We also used fixed stellar masses of 2.25, 2, and 1 $M_\odot$ for SU Aur, RY Tau, and DR Tau, respectively (Cohen & Kuhi 1979; Kenyon et al. 1994); note that the stellar mass is not a critical parameter in the near-infrared. The disk properties, such as mass, accretion rate, and inclination, were varied in order to produce a grid of synthetic SEDs. These models allowed us to explore likely parameter configurations.

### 5.2. Visibility Calculation

To calculate model visibilities, a simulated $K$-band image was created using the Monte Carlo models with pixel size of 0.05 mas and a width of 12.5 mas. The pixel size was chosen to be much smaller than the fringe spacing of 4 mas, and the total

size was a compromise between calculation time (large images are computationally intensive) and capturing the relevant structure. The outer size is large enough to contain any component that would contribute substantially to the model visibility. For example, a thin ring with an inner radius of 3 mas has $V^2 = 0.01$ on the shortest PTI baseline. The $K$-band emission in the models is dominated by structures a few mas in size or less (Fig. 4). As discussed in § 4, any emission within the 1″ FOV will contribute incoherently. To calculate the extended component in the model, a larger image is also constructed with 2 mas pixels and a 1″ field. The emission outside the central 12 mas is calculated and included in the visibility calculation as an incoherent contribution. The effects of the 1″ Gaussian FOV and the finite fringe envelope are also included in the visibility calculation. For each PTI baseline, the model visibility, including the incoherent flux, was calculated for the average baseline length and position angle using the Fourier transform of the image, assuming a position angle for the disk as given in § 4. We thus "observe" the models as they would be observed at PTI.

The model visibilities and full SEDs were then compared to the data presented in § 3.1 and SED data taken from the literature. The optical and infrared SED data are taken from the compilation of Kenyon & Hartmann (1995) and are not contemporaneous but instead represent an average for each source, and the millimeter data are taken from Akeson et al. (2002) and Beckwith et al. (1990). For each object, a set of models was calculated to explore the disk parameters in order to find a viable model, and a sample selection of models for each object is given in Table 6. The parameter space chosen for the inclination angle was restricted using the results from the geometric fits. The model with the total lowest $\chi^2$ is shown for each object in Figure 4 and the corresponding SED fit in Figure 5.

### 5.3. Other Emission Components

Before discussing the results of the Monte Carlo models, we discuss other possible physical components that have not been included in our models. As discussed in § 4, a binary companion would contribute coherently or incoherently to the measured visibility, depending on the separation from the primary. RY Tau was classified as a "variability-induced mover" from *Hipparcos* data, and Bertout (1999) found a solution in which the possible companion had a minimum separation of 24 mas. However, the $K$-band speckle interferometry survey of Leinert et al. (1993) did not detect a companion for RY Tau in the angular range of 0″.1 to 10″, and *Hubble Space Telescope* (*HST*) archival images of RY Tau from WFPC2 show only a single point source. For the incoherent contribution from a companion to account entirely for the measured visibility, the $K$-band flux ratio would range from 0.81 to 1.44 (secondary/primary) for the three baselines, but this could not account for the change in visibility with baseline length and orientation.

Another likely contributor of infrared emission is a circumstellar envelope. An envelope can be a source of scattered and thermally reprocessed starlight and can also veil emission from the central star and accretion disk (see, e.g., the models of Calvet et al. 1997; Whitney et al. 2003a). However, SU Aur, DR Tau, and RY Tau are all class II T Tauri stars and have visual extinctions ≲2. In general, class II sources are thought to have little or no envelope remaining (see, e.g., Mundy et al. 2000). RY Tau shows near-infrared CO lines in absorption (Najita et al. 2003), which Calvet et al. (1997) cite as evidence of no substantial envelope for other class II sources.

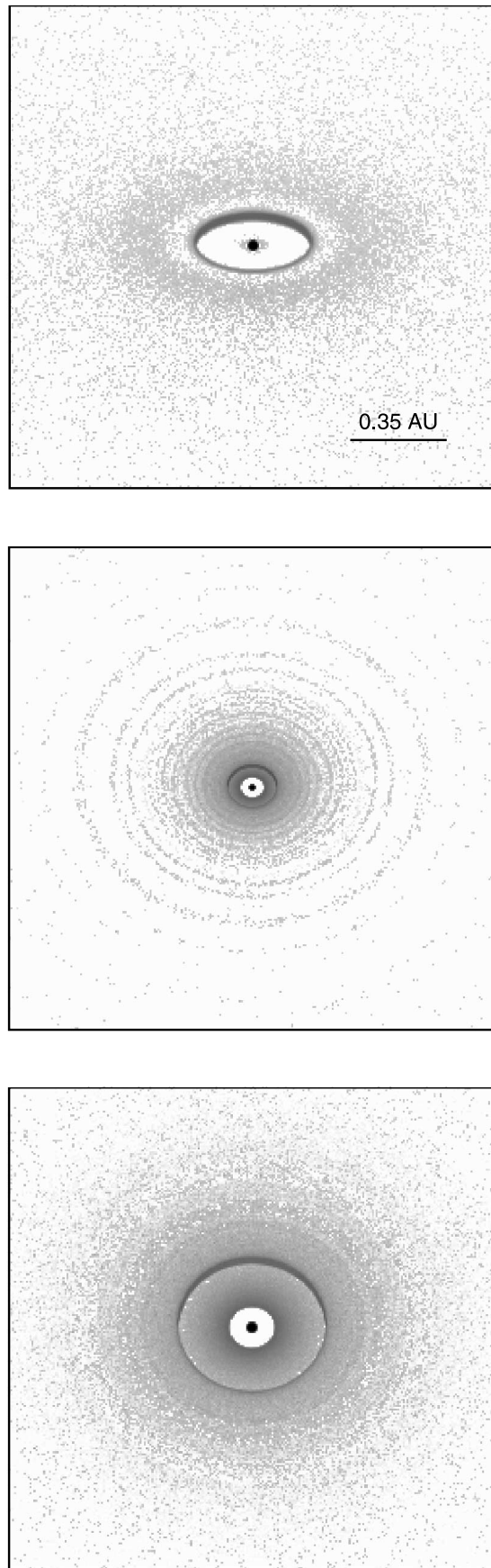To assess the possible presence of emission within the 1″ PTI FOV, we examined *HST* archival images from the standard



Fig. 4.—Model images for SU Aur (*top*), DR Tau (*middle*), and RY Tau (*bottom*). The flux has been scaled to the 0.15 power to provide better contrast in the image. Each image is 12.5 mas or 1.75 AU across. For comparison, all models are shown with the same position angle.

TABLE 6
Representative Model Parameters for Each Source

| Model[a] | $\dot{M}$ ($M_\odot$ yr$^{-1}$) | $r_{\rm in}$ (AU) | $M_{\rm disk}$ ($M_\odot$) | Inclination (deg) | $L_{\rm acc} + L_{\rm shk}$ ($L_\odot$) | $\chi^2_{\rm PTI}$ | $\chi^2_{\rm SED}$ | $\chi^2_{\rm total}$ | Notes |
|---|---|---|---|---|---|---|---|---|---|
| | | | | SU Aur | | | | | |
| SU-A .............. | $1 \times 10^{-9}$ | 0.21 | 0.001 | 60 | 0.02 | 7 | 118 | 125 | |
| SU-B .............. | $1 \times 10^{-9}$ | 0.21 | 0.001 | 50 | 0.02 | 29 | 101 | 130 | |
| SU-C .............. | $1 \times 10^{-9}$ | 0.22 | 0.001 | 50 | 0.02 | 60 | 198 | 258 | |
| SU-D .............. | $2 \times 10^{-9}$ | 0.21 | 0.001 | 50 | 0.02 | 48 | 163 | 211 | |
| SU-E .............. | $4 \times 10^{-9}$ | 0.24 | 0.005 | 50 | 0.02 | 99 | 893 | 992 | |
| | | | | DR Tau | | | | | |
| DR-A.............. | $8 \times 10^{-8}$ | 0.09 | 0.16 | 30 | 1.3 | 12 | 24 | 36 | $R_{\rm gas} = 2R_*$ |
| DR-B .............. | $8 \times 10^{-8}$ | 0.09 | 0.16 | 30 | 1.3 | 30 | 19 | 49 | |
| DR-C .............. | $8 \times 10^{-8}$ | 0.09 | 0.12 | 30 | 1.3 | 30 | 59 | 89 | |
| DR-D.............. | $6 \times 10^{-8}$ | 0.09 | 0.15 | 60 | 0.97 | 9 | 55 | 63 | |
| DR-E .............. | 0 | 0.08 | 0.08 | 60 | 0 | 3 | 82 | 85 | no accretion |
| | | | | RY Tau | | | | | |
| RY-A .............. | $2.5 \times 10^{-7}$ | 0.27 | 0.015 | 25 | 4.28 | 8 | 37 | 45 | |
| RY-B.............. | $3 \times 10^{-7}$ | 0.27 | 0.015 | 25 | 5.13 | 1 | 294 | 295 | |
| RY-C.............. | $2 \times 10^{-7}$ | 0.27 | 0.012 | 25 | 3.42 | 135 | 31 | 166 | |
| RY-D .............. | $2.5 \times 10^{-7}$ | 0.27 | 0.015 | 25 | 4.28 | 4 | 145 | 149 | no gas |
| RY-E............... | $2.5 \times 10^{-7}$ | 0.27 | 0.015 | 25 | 4.28 | 36 | 313 | 349 | envelope |

Note.—The $\chi^2$ values given have *not* been normalized by the degrees of freedom.
[a] The best-fit model is listed first.

imaging pipeline. For each source, we found WFPC2 images taken with the F814W filter on the Planetary Camera CCD. No extended emission or additional sources were apparent in the images; however, they are dominated by the central point source. Azimuthal brightness averages were computed for comparison to a star extracted from the point-spread function (PSF) archive. The core of RY Tau was saturated to such an extent that we were unable to find a matching saturated PSF for comparison. Although the scatter in the PSF averages do not allow a precise comparison, especially in the core, SU Aur and DR Tau are dominated by a central source (Fig. 6). This contrasts with the images of class I sources, such as the sample imaged by Padgett et al. (1999), which show images dominated by scattered light from circumstellar material hundreds of AU in extent. Coronagraphic techniques have revealed some extended emission in RY Tau (Nakajima & Golimowski 1995) and SU Aur (Chakraborty & Ge 2004), but as detailed in § 5.4, this emission is unlikely to contribute substantially in the near-infrared. We have also calculated an example model with a disk and an envelope for RY Tau (§ 5.4.3).

### 5.4. Results

As the wavelength range used for the SED comparison ranges from 0.365 $\mu$m to 3 mm, the model SED is sensitive to many model parameters, from the extinction to the outer disk size and mass. As expected, the infrared visibility is sensitive to only a few model parameters, particularly the inner radius, the inclination angle, and the luminosity. Each object is considered separately below, but the general conclusion is that these models, which include the contribution from extended emission, support the simple geometric models in the large value of $R_{\rm dust}$ found for RY Tau and SU Aur. In part, this is because the models contain incoherent contributions at 2 $\mu$m (here defined as flux from scales greater than 10 mas), which were less than 6% for all sources and could still reproduce both the SED and the

infrared interferometry observations. High-resolution infrared imaging observations would further constrain the extended emission component of these models. The *K*-band excess flux from the models is also close to the veiling values used in § 4, with $F_{\rm excess}/F_{\rm total}$ values of 0.4, 0.74, and 0.68, respectively, for SU Aur, DR Tau, and RY Tau.

The second general conclusion is that emission from gas within $R_{\rm dust}$ is a significant component of the near-infrared emission if $R_{\rm dust}$ is large. For our three objects, this is most evident in the RY Tau model. The relative flux of the gas and dust components for RY Tau can be seen in Figure 7, which shows a cut through the model image with the inner dust wall facing the observer on the left in the plot. In comparison, for the DR Tau model a smaller $R_{\rm dust}$ is necessary to match the high visibilities measured at PTI, and so $R_{\rm dust}$ and $R_{\rm gas}$ are similar. For DR Tau, a smaller value of $R_{\rm gas}$ than was estimated from the stellar properties ($2R_*$ instead of $5R_*$) was necessary to match the data. We have not explored the value of $R_{\rm gas}$ extensively in these models, so these values should be taken as approximate. Observations by Najita et al. (2003) of CO fundamental emission for several single T Tauri stars similar to our targets (e.g., BP Tau) found the inner CO radius to be smaller than the calculated corotation radius for five out of six sources, with CO inner radii of 0.02– 0.09 AU. Modeling of Herbig Ae/Be sources by Muzerolle et al. (2004) found that emission from the inner gas exceeded the stellar emission for accretion rates $>10^{-7}$ $M_\odot$ yr$^{-1}$.

To confirm the effect of the gas emission, a model was constructed for RY Tau in which the gas was artificially removed from the region within $R_{\rm dust}$, which was set to match the measured PTI visibilities. However, the SED fit for this model (Table 6, model RY-D) is not as good as for the model with gas emission.

#### 5.4.1. *SU Aur*

For SU Aur, both the SED and the measured visibilities are well fit by model SU-A. Figure 4 shows the inner region of this
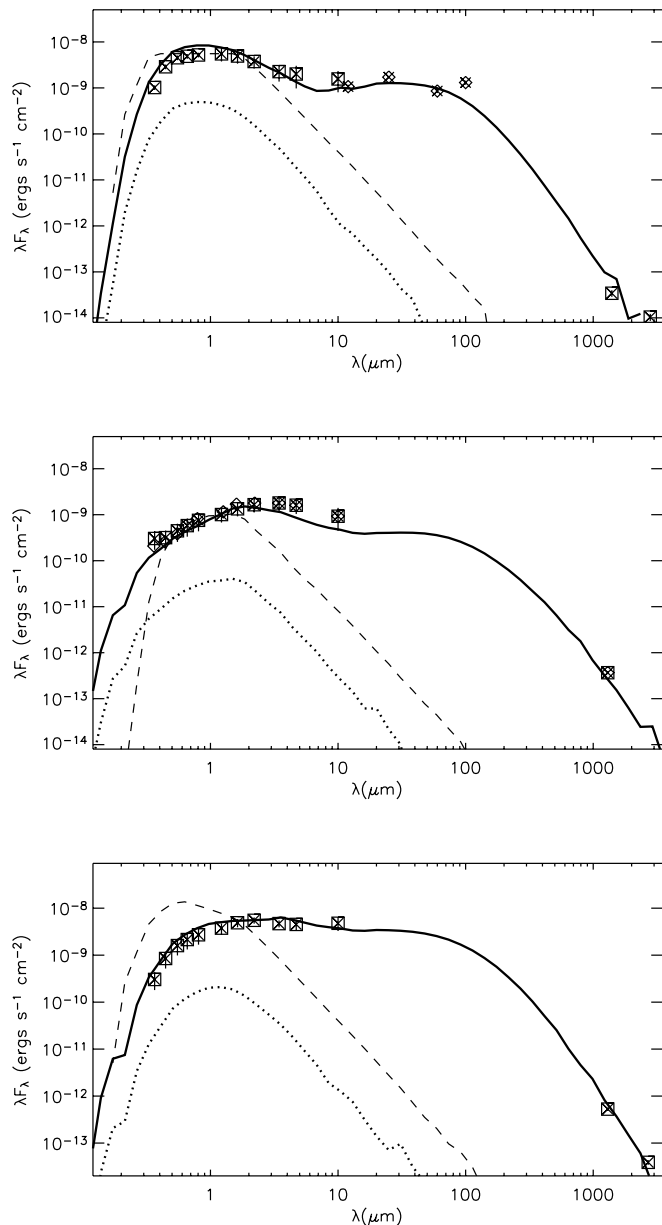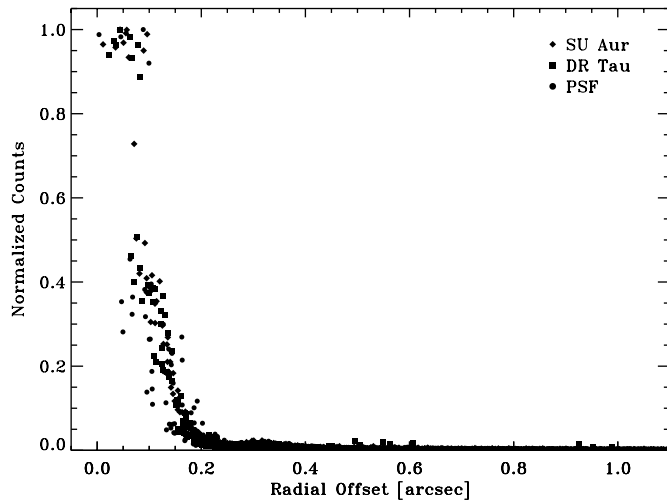
FIG. 6.—Azimuthal averages from *HST* archival images for SU Aur (*diamonds*), DR Tau (*squares*), and a PSF standard (*circles*), all using the F814W filter. For comparison, each source is self-scaled to the peak brightness. [*See the electronic edition of the Journal for a color version of this figure.*]

### 5.4.2. *DR Tau*

It was not possible to fit both the PTI data and the SED data well with these models. The best-fit model listed in Table 6 underestimates the infrared visibility and the SED throughout the near and mid-infrared (Fig. 5). In order to produce an inner disk radius small enough to fit the PTI data, the model must contain no accretion (model DR-E), which drastically underestimates the SED and disagrees with the accretion diagnostics observed for the source (Kenyon et al. 1994; Muzerolle et al. 2003). The infrared photometry (Table 4) does not reveal recent substantial variations; however, the optical veiling for DR Tau has been highly variable (Gullbring et al. 2000), and as the SED data and PTI measurements are not contemporaneous, there may be issues with source variability in our modeling. In addition, note that the models in Table 6 have a lower inclination

FIG. 5.—SED plots for best-fit models for SU Aur (*top*), DR Tau (*middle*), and RY Tau (*bottom*). The model total flux is given by the solid line, the input stellar spectrum by the dashed line, and the scattering by the dotted line. Data from Kenyon & Hartmann (1995) are given by squares and those from Eiroa et al. (2002) by diamonds.

model, with the star and the inner dust disk edge producing the *K*-band emission. At an inclination angle of $60°$, the inner edge of the dust disk facing the observer is clearly brighter. We find $R_{dust} = 0.21$ AU, similar to the inclined ring model radius of 0.18 AU from Table 5. The gas emission is visible close to the star ($R_{gas} = 2R_*$), but the emission is limited by the small surface area at this radius.

Recent observations by Chakraborty & Ge (2004) have traced extended emission at *K* out to radii of 2″.6. This study did not measure the scattered light within 1″, so it does not help constrain the PTI data but does suggest that a complete model for SU Aur would include an extended scattered component; however, their measured *K* flux from 1″ to 2″.6 was only 4% of the 2MASS *K* flux, so neglecting this component adds only a small error to the SED fit.
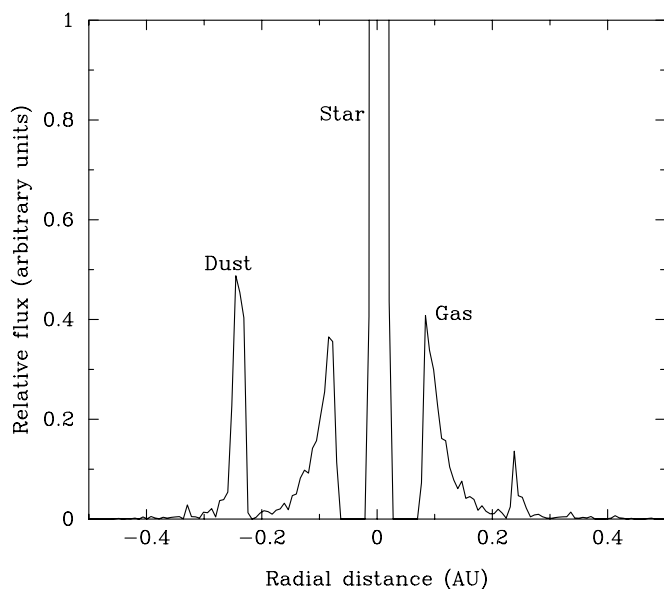


FIG. 7.—A cross section of the RY Tau model through the center of the source showing the relative flux contributions of the gas and dust emission. The slice is oriented such that the inner dust wall facing the observer is on the left.

($30°$) than is given by the geometric fits ($60° \pm 30°$) but is within the uncertainty.

We compared the photometry from Kenyon & Hartmann (1995), which are averages of measurements from the literature, to the optical and infrared contemporaneous SED from Eiroa et al. (2002), and the main deviation is slightly lower fluxes at $u$, $b$, $v$ for the contemporaneous SED, which does not improve our model fits. In the variability study by Skrutskie et al. (1996), DR Tau showed no trend in color with brightness changes, suggesting that the variability is not due to large extinction changes. The variability of DR Tau has been modeled as a hot spot on the stellar photosphere by Kenyon et al. (1994), but the models here do not attempt to model DR Tau with that level of detail.

### 5.4.3. RY Tau

RY Tau has the largest $R_{dust}$ of the three sources, and gas within $R_{dust}$ contributes substantially to the infrared emission. This second component in the disk emission means that the simple ring model is an *underestimate* of $R_{dust}$. Although this same gas component is present in the models for all three sources, the contribution to the $K$-band flux is largest for RY Tau, as $R_{dust}$ is larger than for the other two sources. For RY Tau, the best-fit model was relatively close to the optimal parameters for both the PTI and SED data. The PTI data are best modeled by a higher total luminosity and accretion rate (model RY-B) than the SED data.

A reflection nebulosity has been observed extending to $\sim 40''$ from RY Tau at visible wavelengths. However, this is unlikely to contribute substantially at $K$, as the reflection component is only 2% of the total flux at 0.9 $\mu$m, and scattering decreases with increasing wavelength. To test the effect of an envelope on the predicted visibilities and SED, a model was calculated using the disk properties of model RY-A with an envelope using the same gas and dust radii, 0.01 times the disk mass, and an infall rate of $1 \times 10^{-7}\ M_{\odot}\ yr^{-1}$ for the envelope. As seen in Table 6, this model does not fit either the SED or the visibilities as well. Other models with higher envelope masses were also calculated and had even worse fits to the SED. It may be possible to better match the SED with a different disk and envelope combination; however, we found no observational evidence for substantial near-infrared emission from an envelope.

We note that Calvet et al. (2004) have recently characterized RY Tau as a G1 star, substantially earlier than previous spectral type determinations. However, their stellar properties ($R_* = 2.9\ R_{\odot}$, $M_* = 2.0\ M_{\odot}$) agree reasonably well with the values we used (Table 1). We used a slightly lower effective temperature (5782 K compared to 5945 K) and a higher luminosity (12.8 $L_{\odot}$ compared to 9.6 $L_{\odot}$). A lower stellar luminosity would require a more massive disk and higher accretion to produce the same flux at longer wavelengths, but the general properties of a large $R_{dust}$ would not change. The accretion rate of the model presented here, $2.5 \times 10^{-7}\ M_{\odot}\ yr^{-1}$, is actually higher than the Calvet et al. (2004) estimate of $(6.4–9.1) \times 10^{-8}\ M_{\odot}\ yr^{-1}$.

## 6. CONCLUSIONS

Infrared interferometric observations of T Tauri stars are used to constrain the inner disk properties. Detailed models were presented for SU Aur, RY Tau, and DR Tau to reproduce both the interferometry observations and the spectral energy distribution. For both the simple geometric fits to the interferometry data and the Monte Carlo disk models that include accretion and scattering, the inner dust radius ranges from 0.05 to 0.3 AU. Extended envelopes were not needed to reproduce the SED for these sources, although additional high-resolution infrared images would help in constraining the extended emission on larger scales (tens to hundreds of AU). However, the significant variations in the visibility with baseline length and orientation seen for SU Aur and RY Tau require a resolved component to be present, as an extended component produces a constant visibility reduction. Although the model parameters given here may not be a unique solution to the data set used, they are consistent with the domination of the near-infrared excess by thermal emission from the disk, as expected for class II sources.

The SU Aur model agrees well with the size derived from geometric fits to the interferometer data alone. The SED and PTI visibilities for DR Tau cannot both be fit with these models, perhaps because of source variability. For RY Tau, the model predicts significant emission in the $K$ band from gas within the inner dust disk radius. This gas emission at infrared wavelengths is generally not considered in the simple models used to fit interferometric data, and when this emission is present it results in an underestimate of the dust radius when using a simple ring model.

Future work will extend the observational database to study more sources and probe the innermost regions of disks. Interferometric observations at a second wavelength would add additional constraints on the inner disk structure. From a theoretical perspective, we are extending the Monte Carlo codes to include gas opacity in the inner disk and self-consistently calculate its structure. The data and models presented in this paper clearly show that inner gas disks cannot be ignored and are required when fitting observations that probe the inner regions of disks.

REFERENCES

Akeson, R. L., Ciardi, D. R., van Belle, G. T., & Creech-Eakman, M. J. 2002, ApJ, 566, 1124
Akeson, R. L., Ciardi, D. R., van Belle, G. T., Creech-Eakman, M. J., & Lada, E. A. 2000, ApJ, 543, 313 (Paper 1)
Akeson, R. L., Koerner, D. W., & Jensen, E. L. N. 1998, ApJ, 505, 358
Beckwith, S. V. W., Sargent, A. I., Chini, R. S., & Guesten, R. 1990, AJ, 99, 924
Bertout, C. 1989, ARA&A, 27, 351
Bertout, C., Robichon, N., & Arenou, F. 1999, A&A, 352, 574
Bjorkman, J. E., & Wood, K. 2001, ApJ, 554, 615
Boden, A. F., Colavita, M. M., van Belle, G. T., & Shao, M. 1998, Proc. SPIE, 3350, 872
Calvet, N., & Gullbring, E. 1998, ApJ, 509, 802
Calvet, N., Hartmann, L., & Strom, S. E. 1997, ApJ, 481, 912
Calvet, N., Muzerolle, J., Briceño, C., Hernández, J., Hartmann, L., Saucedo, J. L., & Gordon, K. D. 2004, AJ, 128, 1294
Chakraborty, A., & Ge, J. 2004, AJ, 127, 2898
Cohen, M., & Kuhi, L. V. 1979, ApJS, 41, 743
Colavita, M. M., et al. 1999, ApJ, 510, 505
D'Alessio, P. 2004, in IAU Symp. 221, Star Formation at High Angular Resolution, ed. M. Burton, R. Jayawardhana, & T. Bourke (San Francisco: ASP), 256
Dullemond, C. P., Dominik, C., & Natta, A. 2001, ApJ, 560, 957
Duschl, W. J., Gail, H.-P., & Tscharnuter, W. M. 1996, A&A, 312, 624
Eiroa, C., et al. 2002, A&A, 384, 1038
Eisner, J. A., Lane, B. F., Hillenbrand, L. A., Akeson, R. L., & Sargent, A. I. 2004, ApJ, 613, 1049
Folha, D. F. M., & Emerson, J. P. 1999, A&A, 352, 517
Ghosh, P., & Lamb, F. K. 1979, ApJ, 234, 296
Gomez de Castro, A. I., & Franqueira, M. 1997, ApJ, 482, 465
Gullbring, E., Calvet, N., Muzerolle, J., & Hartmann, L. 2000, ApJ, 544, 927
Herbig, G. H., & Bell, K. R. 1988, Lick Obs. Bull. 111, Third Catalog of Emission-line Stars for the Orion Population (Santa Cruz: Univ. California)
Kenyon, S. J., & Hartmann, L. 1995, ApJS, 101, 117
Kenyon, S. J., et al. 1994, AJ, 107, 2153
Kitamura, Y., Momose, M., Yokogawa, S., Kawabe, R., Tamura, M., & Ida, S. 2002, ApJ, 581, 357
Koenigl, A. 1991, ApJ, 370, L39
Koerner, D. W., & Sargent, A. I. 1995, AJ, 109, 2138
Koresko, C. D. 2000, ApJ, 531, L147
Kurucz, R. L. 1994, Kurucz CD-ROM 19, Solar Abundance Model Atmospheres for 0, 1, 2, 4, 8 km/s (Cambridge: SAO)
Landolt, A. U. 1992, AJ, 104, 340
Leinert, C., Zinnecker, H., Weitzel, N., Christou, J., Ridgway, S. T., Jameson, R., Haas, M., & Lenzen, R. 1993, A&A, 278, 129

Lynden-Bell, D., & Pringle, J. E. 1974, MNRAS, 168, 603
Malbet, F., et al. 1998, ApJ, 507, L149
Millan-Gabet, R., Schloerb, F. P., & Traub, W. A. 2001, ApJ, 546, 358
Millan-Gabet, R., Schloerb, F. P., Traub, W. A., Malbet, F., Berger, J. P., & Bregman, J. D. 1999, ApJ, 513, L131
Monnier, J. D., & Millan-Gabet, R. 2002, ApJ, 579, 694
Mundy, L. G., Looney, L. W., & Welch, W. J. 2000, in Protostars and Planets IV, ed. V. Mannings, A. P. Boss, & S. S. Russell (Tucson: Univ. Arizona Press), 355
Muzerolle, J., Calvet, N., Hartmann, L., & D'Alessio, P. 2003, ApJ, 597, L149
Muzerolle, J., D'Alessio, P., Calvet, N., & Hartmann, L. 2004, ApJ, 617, 406
Najita, J., Carr, J. S., & Mathieu, R. D. 2003, ApJ, 589, 931
Nakajima, T., & Golimowski, D. A. 1995, AJ, 109, 1181
Natta, A., Prusti, T., Neri, R., Wooden, D., Grinin, V. P., & Mannings, V. 2001, A&A, 371, 186
Padgett, D. L., Brandner, W., Stapelfeldt, K. R., Strom, S. E., Terebey, S., & Koerner, D. 1999, AJ, 117, 1490
Pringle, J. E. 1981, ARA&A, 19, 137
Rice, W. K. M., Wood, K., Armitage, P. J., Whitney, B. A., & Bjorkman, J. E. 2003, MNRAS, 342, 79
Schneider, G., Wood, K., Silverstone, M. D., Hines, D. C., Koerner, D. W., Whitney, B. A., Bjorkman, J. E., & Lowrance, P. J. 2003, AJ, 125, 1467
Shu, F., Najita, J., Ostriker, E., Wilkin, F., Ruden, S., & Lizano, S. 1994, ApJ, 429, 781
Simon, M., Beck, T. L., Greene, T. P., Howell, R. R., Lumsden, S., & Prato, L. 1999, AJ, 117, 1594
Skrutskie, M. F., Meyer, M. R., Whalen, D., & Hamilton, C. 1996, AJ, 112, 2168
Stapelfeldt, K. R., et al. 1998, ApJ, 508, 736
Tuthill, P. G., Monnier, J. D., & Danchi, W. C. 2001, Nature, 409, 1012
Unruh, Y. C., et al. 2004, MNRAS, 348, 1301
White, R. J., & Ghez, A. M. 2001, ApJ, 556, 265
Whitney, B. A., Wood, K., Bjorkman, J. E., & Cohen, M. 2003a, ApJ, 598, 1079
Whitney, B. A., Wood, K., Bjorkman, J. E., & Wolff, M. J. 2003b, ApJ, 591, 1049
Wood, K., Kenyon, S. J., Whitney, B. A., & Bjorkman, J. E. 1996, ApJ, 458, L79
Wood, K., Lada, C. J., Bjorkman, J. E., Kenyon, S. J., Whitney, B., & Wolff, M. J. 2002a, ApJ, 567, 1183
Wood, K., Smith, D., Whitney, B., Stassun, K., Kenyon, S. J., Wolff, M. J., & Bjorkman, K. S. 2001, ApJ, 561, 299
Wood, K., Wolff, M. J., Bjorkman, J. E., & Whitney, B. 2002b, ApJ, 564, 887